

## Adsorption of diferrocenylacetylene on Au(111) studied by scanning tunneling microscopy

Cite this: *Phys. Chem. Chem. Phys.*, 2013, **15**, 6973

Rebecca C. Quardokus,<sup>a</sup> Natalie A. Wasio,<sup>a</sup> Ryan P. Forrest,<sup>a</sup> Craig S. Lent,<sup>b</sup> Steven A. Corcelli,<sup>a</sup> John A. Christie,<sup>a</sup> Kenneth W. Henderson<sup>a</sup> and S. Alex Kandel\*<sup>a</sup>

Scanning tunneling microscopy images of diferrocenylacetylene (DFA) coadsorbed with benzene on Au(111) show individual and close-packed DFA molecules, either adsorbed alongside benzene or on top of a benzene monolayer. Images acquired over a range of positive and negative tip-sample bias voltages show a shift in contrast, with the acetylene linker appearing brighter than the ferrocenes at positive sample bias (where unoccupied states primarily contribute) and the reverse contrast at negative bias. Density functional theory was used to calculate the electronic structure of the gas-phase DFA molecule, and simulated images produced through two-dimensional projections of these calculations approximate the experimental images. The symmetry of both experimental and calculated molecular features for DFA rules out a *cis* adsorption geometry, and comparison of experiment to simulation indicates torsion around the inter-ferrocene axis between 90° and 180° (*trans*); the cyclopentadienyl rings are thus angled with respect to the surface.

Received 17th January 2013,

Accepted 18th March 2013

DOI: 10.1039/c3cp50225b

[www.rsc.org/pccp](http://www.rsc.org/pccp)

Since its first description in the literature in 1951,<sup>1</sup> the unique geometry and stability of ferrocene [Fe(C<sub>5</sub>H<sub>5</sub>)<sub>2</sub>] have made it a focus for investigation and a promising candidate for potential use in a variety of applications, including medicine,<sup>2–4</sup> materials,<sup>5,6</sup> and catalysis.<sup>7–10</sup> The two aromatic 5-membered cyclopentadienyl (Cp) rings sandwiching an iron center, in a +2 oxidation state, makes for a very stable metallocene, and this, along with the electronic characteristics of ferrocene and diferrocene complexes, makes ferrocene-based molecules interesting targets of study. Our particular interest in molecular electronic devices has led us to explore diferrocene complexes, which can be produced in mixed-valence oxidation states.<sup>11–16</sup> Many studies, looking for potential candidates for use in molecular electronic devices, have focused on the intramolecular charge distribution of dinuclear organometallic molecules.<sup>16–26</sup> For such applications, as well as for applications in materials and catalysis, it is important to have a fundamental understanding of ferrocene-based molecules as molecular adsorbates on surfaces.

A number of studies have been done to characterize the substrate-adsorbate interactions of ferrocene and ferrocene-based molecules on metal surfaces.<sup>27–30</sup> The orientation and packing of ferrocene on a surface appears to be substrate dependent.

Ensemble measurements have shown that ferrocene physisorbs with the Cp ring parallel to the surface on Ag(100) and with the Cp ring perpendicular to a Cu(100) surface.<sup>31–33</sup> A study by Zhong *et al.* has reported ferrocene attached to organic chains that adsorb on Cu(110) with the ferrocenyl group in both orientations, and even switching orientation from parallel to perpendicular between scans with a scanning tunneling microscope (STM).<sup>34</sup> It has been reported that ferrocene dissociates when physisorbed to Au(111) at room temperature.<sup>35</sup> Low-temperature STM studies show that ferrocene nondissociatively physisorbs to a Cu(111) surface.<sup>36</sup> Manipulation of ferrocene groups with the tip of an STM in a diferrocene complex have reported dissociation of ferrocene resulting in a stronger Fe-surface interaction on Cu(110).<sup>37</sup> It has also been reported that the packing and orientation of the ferrocene end groups becomes more complex when organic chains and linker groups are added to the ferrocene base.<sup>27–30</sup>

Here we report on an STM investigation of diferrocenylacetylene (DFA) on Au(111). DFA, shown in Fig. 1, consists of two ferrocene molecules joined together with an acetylene linker between the cyclopentadienyl rings. In the neutral molecule, both of the iron centers in DFA are in the +2 oxidation state, though DFA can also be oxidized to create a mixed-valence +2/+3 complex.<sup>11–13</sup> As part of a longer-range plan to investigate mixed-valence DFA, as well as more complex organometallic systems based upon it,<sup>38</sup> we are interested in preparing molecules in a solution environment before deposition on a solid surface. With this approach, solvent

<sup>a</sup> Department of Chemistry and Biochemistry, University of Notre Dame, Notre Dame, IN 46556, USA. E-mail: skandel@nd.edu

<sup>b</sup> Department of Electrical Engineering, University of Notre Dame, Notre Dame, IN 46556, USA

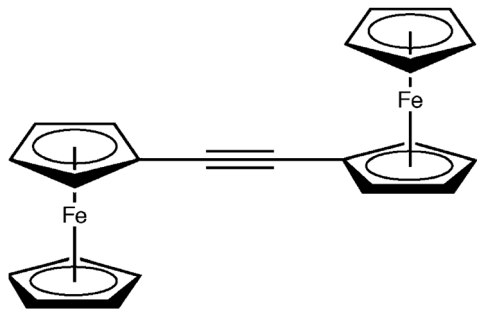


Fig. 1 Structure of diferrocenylacetylene (DFA).

molecules are necessarily deposited on the surface alongside solutes;<sup>39</sup> here, benzene is co-deposited with DFA. The result is a fairly complex surface arrangement of molecules, and solvent coadsorption can potentially modify the interaction of solute molecules with the surface and with each other. This can result in the promotion of certain adsorption geometries, a change in the relative degree of ordering, or a modification of the electronic coupling between the surface and adsorbates. Depending on the application, the effects of solvent can be either beneficial or detrimental, and we begin to characterize these effects here in order to understand the nature of intermolecular and molecule-surface interactions. Additionally, studying co-deposition of DFA and benzene on Au(111) lays a foundation that will aid in the interpretation of more complex structures and systems.

## I. Experimental

### A. Synthesis

**1. General considerations.** All manipulations were carried out using standard Schlenk techniques under a nitrogen ( $N_2$ ) atmosphere. Unless otherwise mentioned, reagents and solvents were used as purchased.  $^1H$  NMR spectra were recorded on a Varian-300 spectrometer at 293 K and were referenced internally to the residual signals of the deuterated solvent. Tetrahydrofuran (THF) and hexane were purified by passage through a solvent purification system (Innovative Technology). Benzene was refluxed over molten potassium overnight before distilling onto 4 Å molecular sieves under  $N_2$ . Pyridine and ethanol were deoxygenated overnight with  $N_2$ . Diisopropylamine was distilled over  $CaH_2$  and stored over 4 Å molecular sieves. Copper iodide was purified by standard procedure.<sup>40</sup>

**2. Synthesis of iodoferrocene.** The synthesis of iodoferrocene follows a modified literature procedure.<sup>41</sup> A flame-dried Schlenk flask was charged with ferrocene (15.8 g, 85 mmol), THF (40 mL) and hexane (40 mL). The resulting solution was cooled in an ice bath. A pentane solution of  $^tBuLi$  (100 mL, 1.7 M, 170 mmol) was added dropwise *via* cannula over the course of 90 minutes and left to stir for 30 additional minutes at 0 °C. Then,  $^nBu_3SnCl$  (35 mL, 128 mmol) was added over 20 minutes and the solution was allowed to warm to room temperature over the course of 90 minutes. The solution was then hydrolyzed with aqueous NaOH(aq) (160 mL, 1 M). The product was extracted into diethyl ether, dried over  $MgSO_4$ , concentrated, passed through a silica

column using hexane, and evaporated to a red oil. The (tri-*n*-butylstannyl)ferrocene was isolated by first subliming the unreacted ferrocene from the mixture at 80 °C under vacuum, followed by vacuum distillation at 180 °C to separate the (tri-*n*-butylstannyl)ferrocene and unreacted (tri-*n*-butylstannyl)chloride from the bis(tri-*n*-butylstannyl)ferrocene. The (tri-*n*-butylstannyl)ferrocene mixture was then dissolved in 350 mL  $CH_2Cl_2$  and reacted with iodine (45 g, 94.5 mmol) at room temperature for 24 hours; after which the reaction was washed with 1 M  $Na_2S_2O_3$  and the organic layer was filtered through silica, the  $CH_2Cl_2$  was removed *in vacuo* and the product was dissolved in methanol. Excess KF was added to precipitate (tri-*n*-butyl)stannyl fluoride, the solution was filtered through celite and the product was evaporated to dryness. The product was then extracted into diethyl ether, washed with water, dried over  $MgSO_4$  and evaporated to dryness. The product was then recrystallized from pentane to give 19.73 g of pure reddish brown iodoferrocene (74% yield).  $^1H$  NMR ( $CDCl_3$ )  $\delta$  4.42 (m, 2H), 4.20 (s, 5H), 4.16 (m, 2H).

**3. Synthesis of ethynylferrocene.** The synthesis of ethynylferrocene follows a modified procedure based on ref. 42. Acetylferrocene (16.77 g, 73.53 mmol) was added to a flame dried 500 mL Schlenk flask, dissolved in THF (200 mL) and cooled in a dry ice-acetone bath. In a separate 200 mL flame dried Schlenk flask, diisopropylamine (11.37 mL, 80.88 mmol) in THF (40 mL) was cooled in a dry ice-acetone bath and  $^nBuLi$  (3.35 mL, 2.5 M, 80.88 mmol) was added drop wise. The lithium diisopropylamide (LDA) solution was transferred drop wise *via* cannula to the acetylferrocene solution. The combined solutions were stirred for an additional hour before the reaction was allowed to warm slightly to ensure full reaction and then placed back into the dry ice-acetone bath. Diethylchlorophosphate (10.40 mL, 72.21 mmol) was added drop wise. After stirring for 1 hour, the reaction was warmed to room temperature and placed back into the dry ice-acetone bath. A second portion of LDA was prepared in a flame dried 200 mL Schlenk flask by combining diisopropylamine (23.80 mL, 169.13 mmol), THF (85 mL) and  $^nBuLi$  (67.65 mL, 2.5 M, 169.13 mmol). The second LDA solution was transferred to the acetylferrocene solution drop wise *via* cannula and the reaction was allowed to warm to room temperature before hydrolyzing at 0 °C. The product was extracted into  $CH_2Cl_2$ , washed with water and dried over  $MgSO_4$ . The product was then concentrated *in vacuo* and flushed through silica column with hexane to give 12.18 g (70% yield) of ethynylferrocene as a dark yellow oil.  $^1H$  NMR ( $CDCl_3$ )  $\delta$  4.47 (m, 2H), 4.23 (s, 5H), 4.21 (m, 2H), 2.73 (s, 1H).

**4. Synthesis of copper ferrocenylacetylde.** The procedure described in ref. 43 was modified for the synthesis of copper ferrocenylacetylde. Ethynylferrocene (14.25 g, 67.2 mmol) was dissolved in ethanol (480 mL) and added to a solution of copper iodide (19.20 g, 100.8 mmol) in 360 mL of aqueous ammonia, instantly precipitating a yellow solid. The mixture was stirred for an additional 15 minutes, filtered, washed with aqueous ammonia until the filtrate was colorless and then washed with water. The bright yellow powder was allowed to sit under vacuum to remove any residual ammonia and then dried in an oven at 75 °C overnight to produce 15.9 g of copper ferrocenylacetylde (86% yield).

**5. Synthesis of DFA.** The synthesis of DFA follows a modified literature procedure.<sup>43</sup> Copper ferrocenylacetylde (5.4 g, 20 mmol) and iodoferrocene (8.15 g, 26 mmol) were added to a 250 mL round bottom flask under a N<sub>2</sub> atmosphere. Pyridine (210 mL) was added *via* cannula and the reaction was allowed to reflux for 2 hours before being poured into 400 mL of ice water. The resulting precipitated material was filtered off and dried. This material was then sublimed at 80 °C under vacuum to recover unreacted iodoferrocene (3.4 g) and the remaining material was then sublimed at 180 °C to isolate 4.36 g of bright orange DFA (56% yield). <sup>1</sup>H NMR (CDCl<sub>3</sub>) δ 4.46 (m, 4H), 4.24 (s, 10H), 4.21 (m, 4H).

## B. Sample preparation

Au(111)-on-mica substrates (Agilent Technologies) underwent two rounds of Ar<sup>+</sup> sputtering and annealing at 400 °C in vacuum. A 1 mM solution of diferrocenylacetylene in benzene was prepared and several μL of solution were pulse deposited onto the Au(111) surface in vacuum at room temperature using a pulsed solenoid valve (Parker Instrumentation 9-series, 0.5 mm nozzle diameter, IOTA One driver).<sup>39,44–49</sup> The samples were cooled to 77 K prior to imaging with a low-temperature ultra-high-vacuum scanning tunneling microscope (LT-UHV STM from Omicron NanoTechnology) at pressures below  $3 \times 10^{-10}$  Torr. All images were obtained with the sample bias voltage applied to the sample.

In several experiments, we attempted to chemically oxidize DFA with ferrocenium hexafluorophosphate (FcPF<sub>6</sub>) in benzene. However, we had little success dissolving the oxidizing agent, and consequently the majority of DFA remained in its neutral state: there were no observable differences between samples prepared with and without FcPF<sub>6</sub>. Images shown in Fig. 2, 3, and 10 included trace amounts of FcPF<sub>6</sub> in their sample preparation, while all other samples were prepared only with benzene and DFA.

## II. Electronic structure calculations

Electronic structure calculations were performed on both *cis* and *trans* conformations of DFA using the NWCHEM software package.<sup>50</sup> These calculations were performed with DFT using

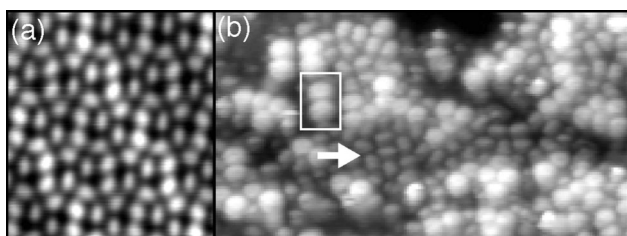


**Fig. 2** (a) Benzene pulse-deposited on Au(111), 65 Å × 70 Å. The bright diagonal stripes are caused by the underlying herringbone reconstruction of Au(111). (b) Attempted oxidation of DFA and benzene pulse deposited on Au(111), 145 Å × 70 Å. The double-dot feature inside of the white box is a DFA molecule and the white arrow is pointing to features that resemble benzene from panel (a). Both images were scanned with a tunneling current of 10 pA and a sample bias voltage of 0.5 V.

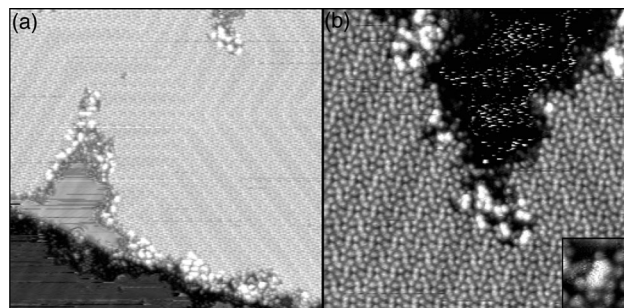


**Fig. 3** (a) 600 Å × 577 Å and (b) 256 Å × 250 Å, attempted oxidation of DFA and benzene co-deposited on Au(111). Images (a) and (b) were taken with a 10 pA tunneling current and −0.5 V sample bias voltage. The benzene monolayer has a complex structure, and DFA is present at the 2D gas phase and 2D solid phase interface.

the B3LYP hybrid exchange–correlation functional. The 6-311G(d,p) basis set was used for all C and H atoms, and the LANL2TZ(f) effective core potential basis set was used for all Fe atoms. Geometries of *cis* and *trans* DFA were optimized imposing *C*<sub>2v</sub> and *C*<sub>2h</sub> symmetries respectively, and were then used to compute the electron densities for various occupied and unoccupied electronic states.

The complexity of the DFA–benzene–Au(111) system produces a number of uncertainties, most notably of the adsorption geometry of the DFA molecule and the number and arrangement of coadsorbed benzene molecules. For this reason, and because we wish in future studies to extend this approach to larger molecules in multiple oxidation states, we did not include the STM tip or the gold surface in the calculations. We have previously found for several organometallic systems that using gas-phase electronic-structure calculations can result in qualitatively accurate results.<sup>17,18</sup> However, the validity of and potential problems with this assumption will be discussed further in the following section.

The electron density of the isolated molecule of interest is integrated over space along the tunneling direction (*z*-axis) to predict the tunneling current,  $I(x, y; V_b)$ , at any location (*x, y*) and bias (*V<sub>b</sub>*) of the STM tip using the following expression,

$$I(x, y; V_b) = \int_{E_F}^{E_F + eV_b} \rho(x, y; E) dE \quad (1)$$

where  $\rho(x, y; E)$  is the reduced electron density of states at energy *E*,

$$\rho(x, y; E) = \sum_i |\Psi_i(x, y, z)|^2 \delta(E - E_i) e^{-\alpha z} dz \quad (2)$$

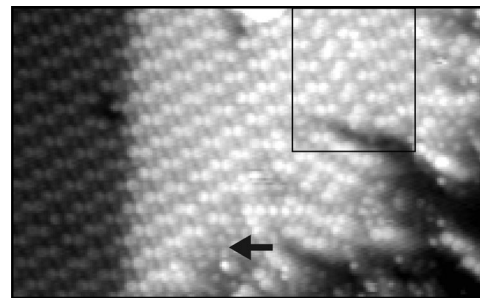
which is obtained from the calculated molecular orbitals,  $\Psi_i(x, y, z)$ , having energy *E<sub>i</sub>*, and *E<sub>F</sub>* is the Fermi level of the substrate. Note that the integration is empirically weighted with an exponential decay factor,  $e^{-\alpha z}$ , ensuring that the electron density closest to the STM tip contributes primarily to the resulting tunneling current, and in accordance with the exponential dependence of tunneling current with distance. In the limit of  $\alpha = 0$ , the Tersoff–Hamann integral is recovered,<sup>51</sup> while large  $\alpha$  values result in a surface of constant local state density. Here we found that good agreement with experimental images resulted from  $\alpha = 0.16 \text{ \AA}^{-1}$ .

### III. Results and discussion

The technique of pulse-deposition allows for large, delicate molecules to remain intact as they are deposited onto a surface.<sup>39,44–49</sup> We have deposited DFA dissolved in benzene, which results in a surface with both solute and solvent molecules coadsorbed, as without post-deposition annealing, even low-boiling-point solvents will remain on the surface at sub-monolayer concentrations.<sup>39</sup> Benzene and DFA are observed in a variety of configurations: we see benzene in both the 2D gas phase and solid phase, DFA sitting on and around benzene, and a partial monolayer of DFA absorbed onto a partial monolayer of benzene. The majority of DFA remains intact when pulse-deposited onto the Au(111) surface. We do not see the same dissociation of ferrocene groups of DFA that Braun *et al.* reported with ferrocene adsorbed on Au(111).<sup>35</sup> It is not impossible that there may exist some dissociated DFA on the surface, but the presence of small impurities and solvent clusters make it difficult to interpret those particular areas of the sample.

After pulse deposition of benzene, STM images consistently show areas of the surface completely covered by benzene monolayers. One such area is shown in Fig. 2a. A complex packing of molecules is evident, with the underlying herringbone reconstruction of the Au(111) surface showing up as diagonal stripes on the image. While images were not required under the highly calibrated, low-drift conditions necessary for an exact lattice assignment, we can characterize the observed periodicity of the benzene lattice in Fig. 2a and 3b. The lattice has rectangular symmetry, with a  $19.2 \times 25.3 \text{ \AA}$  unit cell that contains 12 benzene molecules. Coverage is similar ( $40.4 \text{ \AA}^2$  per benzene) to the high-density  $\sqrt{52} \times \sqrt{52}$  structure reported in ref. 52, though that structure appeared as a nearly perfect hexagonal lattice in STM images. On the other hand, the  $\sqrt{133} \times \sqrt{133}$  structure from ref. 52 shares some structural “pinwheel” motifs with the monolayers we describe here, though it is only observed covering limited areas of the surface, and has a lower density of  $47.8 \text{ \AA}^2$  per benzene. This may be the result of a different coverage regime, or may instead be a consequence of the peculiar physics of droplet evaporation that occurs in pulse deposition.

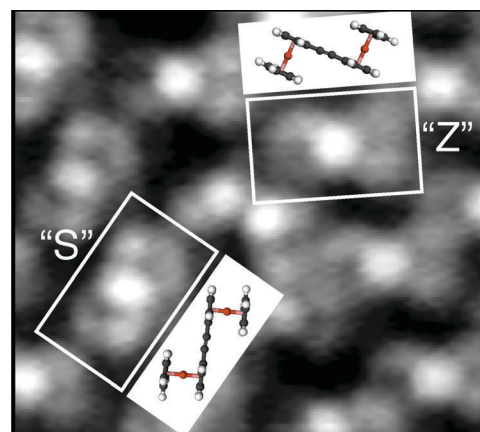
Fig. 2b shows both DFA and benzene co-adsorbed on the Au(111) surface. In this image, DFA appears as a symmetric double-dot feature; the box in Fig. 2b is around one DFA molecule. The arrow in Fig. 2b points to smaller features that closely resemble the benzene from Fig. 2a. In Fig. 3, pulse depositing DFA and benzene has allowed for a partial monolayer of benzene with DFA at the edges. The hazy, noisy area at the lower-mid left of the panel (a) image is characteristic of mobile molecular adsorbates; the STM tip is not able to resolve the molecules, but they show up as “blips” in the image as they pass underneath the tip as it scans.<sup>53,54</sup> Close inspection of both this two-dimensional gas-like phase<sup>55,56</sup> and the two-dimensional ordered benzene monolayer shows that the herringbone reconstruction of Au(111) remains intact under both. DFA can be found along the border between two-dimensional solid- and gas-phase benzene;<sup>52</sup> and individual molecular features (two dots per DFA molecule) are well resolved in Fig. 3b.



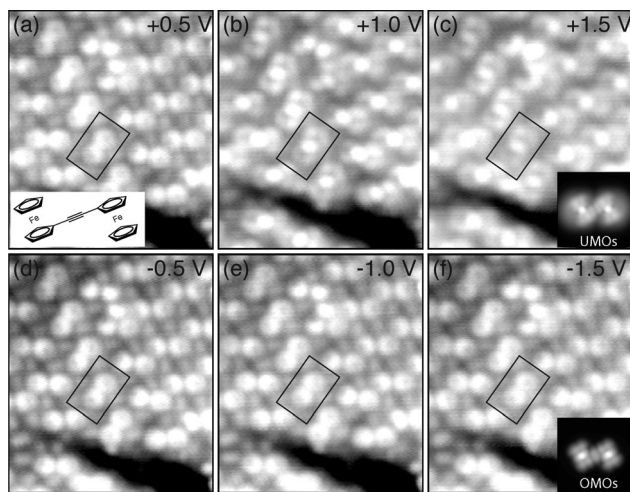
**Fig. 4**  $235 \text{ \AA} \times 140 \text{ \AA}$ , DFA and benzene pulse-deposited onto Au(111). The area inside of the box is the same area of molecules reported on in Fig. 6. The arrow points to small features that resemble benzene, as in Fig. 2 and 3. Benzene appears to be present underneath the partial monolayer of DFA. The image was scanned with a tunneling current of 10 pA and a sample bias voltage of  $-1.0 \text{ V}$ .

Fig. 4 shows a partial monolayer of DFA. At the edges of the region containing close-packed DFA molecules, we see features that match benzene from Fig. 2; an example area is indicated with an arrow. Although it is difficult to definitively assign the features in the image using only STM data, it appears that the benzene monolayer continues underneath the DFA monolayer. Fig. 2–4, then, show that pulse-deposited DFA will sit on, around, and next to benzene on Au(111). In Fig. 4 in particular, it appears that the lattice structure of the benzene is unperturbed by the surrounding DFA, suggesting that the DFA is sitting on top of the benzene monolayer.

STM is able to achieve intramolecular resolution of large molecules, which aids in assigning the geometry of a molecule on a surface.<sup>63,64</sup> Looking carefully at the molecular features in Fig. 5, imaged molecules appear slightly asymmetric, with two mirror-image conformations (“S” and “Z”) adsorbed side by side. The presence of point symmetry opposed to plane symmetry in these images of DFA proves that molecules are neither adsorbed in a perfect *cis* geometry nor a *trans* geometry aligned along the surface normal. STM measurements inherently probe both electronic and topographical surface properties, and adjusting the magnitude and polarity of the sample bias voltage allows for



**Fig. 5**  $45 \text{ \AA} \times 40 \text{ \AA}$ , STM images of a DFA molecule in the “S” configuration and a DFA molecule in the “Z” configuration. The image was scanned with a tunneling current of 10 pA and a sample bias voltage of  $1.0 \text{ V}$ .



**Fig. 6** (a)–(f)  $60 \text{ \AA} \times 70 \text{ \AA}$ , neutral DFA imaged with a 10 pA current and varying sample bias voltages: (a) +0.5 V (b) +1.0 V (c) +1.5 V (d) –0.5 V (e) –1.0 V (f) –1.5 V. A cartoon line-drawing of DFA appears in the bottom right-hand corner of (a). A simulated STM image of the unoccupied molecular orbitals (UMOs), including a combination of the orbitals: LUMO, LUMO + 1, LUMO + 2, and LUMO + 3, appears in the bottom right-hand corner of (c). A simulated STM image of the occupied molecular orbitals (OMOs), including a combination of the orbitals: HOMO, HOMO – 1, HOMO – 2, and HOMO – 3, appears in the bottom right hand corner of (f).

different combinations of filled or empty electronic surface states to be imaged.<sup>65</sup> Fig. 6 shows DFA images taken with varying sample bias voltages. Sub-molecular features are resolved while scanning with both a positive and negative sample bias, though asymmetry of molecular features is pronounced only at positive sample bias voltages. The unoccupied molecular orbitals (UMOs), scanned with positive sample bias voltages in excess of +1.0 V, appear as dim-bright-dim features with an “S” or “Z” shape in Fig. 6b and c. At lower positive biases (Fig. 6a) and negative biases (Fig. 6d–f), both the dim-bright-dim structure and the left-right asymmetry become less pronounced, and the overall molecular features become brighter and somewhat more compact.

The images in Fig. 6 were processed to form lower-noise, higher-contrast composite images. These images, shown in Fig. 7, were generated by overlapping multiple molecular features, iteratively using autocorrelation to optimize their relative translation. The images in panels (a) and (c) were acquired at –0.5 V and are brighter and more compact, while the +1.0 V images in (b) and (d) are larger and more diffuse. In these composite images, broken planar symmetry can also be seen in the negative-bias molecular features.

Comparison with DFT-calculated STM images was used to provide additional insight into the DFA adsorption geometry, and the results of simulated STM images are shown in Fig. 8 and 9. The exact calculation of STM images requires knowledge of how each individual molecular orbital contributes to image contrast, as a function of experimental bias voltage. The energies that result from a gas-phase DFT calculation, however, are approximate only; they do not take into account interaction with the surface, and even for a gas-phase molecule will be inaccurate for unfilled molecular orbitals. A sketch of the calculated

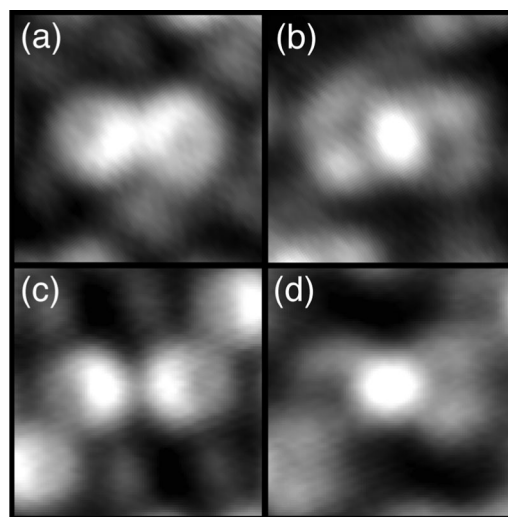


**Fig. 7** (a)–(d)  $16 \text{ \AA} \times 16 \text{ \AA}$  composite images of the DFA in “S” (panels a and b) and “Z” configurations. Images (a) and (c) were scanned using a sample bias voltage of –0.5 V and (b) and (d) using a sample bias voltage of +1.0 V; tunneling current was 10 pA.

energies at the right of Fig. 9 shows a large ( $\sim 4.5 \text{ eV}$ ) HOMO–LUMO gap. Given this, the “tails” of these energies, broadened by adsorption, are what are likely to affect contrast in STM images. We also considered higher-energy unoccupied orbitals (a group of three  $\sim 1 \text{ eV}$  both above the LUMO and below the next-highest energy state) and lower-energy occupied orbitals (three orbitals close in energy to the HOMO, but separated by  $\sim 1 \text{ eV}$  from the next-lowest level).

Based on this, the images in Fig. 8 were simulated from DFT calculations of the highest occupied molecular orbital (HOMO), HOMO – 1, HOMO – 2, and HOMO – 3; and the lowest unoccupied molecular orbital (LUMO), LUMO + 1, LUMO + 2, and LUMO + 3. We combined the four highest occupied molecular orbitals (OMOs) together to calculate the theoretical STM images in the OMOs column of Fig. 8, and the four lowest unoccupied molecular orbitals (UMOs) together to calculate the theoretical STM images in the UMOs column. The ball and stick models demonstrate the orientation of the molecule for each theoretical STM image. Each theoretical image is a birds-eye view of the molecule on the surface. This is a mapping of the electron density of the molecule, similar to what we would expect to see using an STM. The simulated images reproduce the trend observed experimentally: there are larger and more diffuse structure when imaging unoccupied orbitals, and more compact molecular features when imaging occupied orbitals. Of the calculated images, Fig. 8e is the only image of the UMOs to give a “Z” shape that approximates that seen in the experimental images; all other geometries result in plane-symmetric images.

The match between experiment and calculation is by no means quantitative. In particular, the brightness of the acetylene linker is not represented in the theoretical image, and the metal centers are much less prominent in the experimental images. Fig. 9 explores different parameters to better match experiment

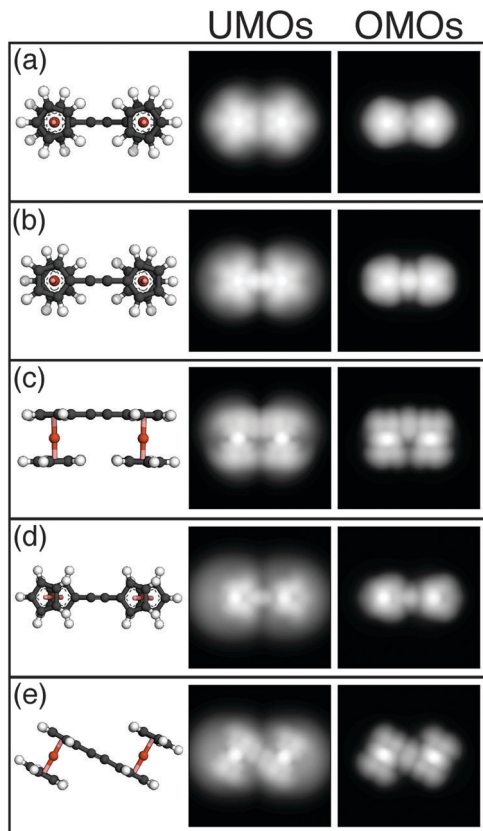


**Fig. 8** (a)–(e) A ball and stick model of DFA next to the theoretical STM images of the UMOs and OMOs for DFA of a particular orientation. (a) *Cis* DFA with the acetylene linker as the base and the Cp rings parallel with the surface. (b) *Cis* DFA with the Cp rings parallel to the surface but with the acetylene linker sitting off of the surface. (c) *Cis* DFA with Cp rings perpendicular to the surface. (d) *Trans* DFA with the Cp rings and the acetylene linker at an angle to the surface. (e) *Trans* DFA creating a “Z” shape with the Cp rings perpendicular to the surface.

to simulation. First, the energy-state-averaged simulations are compared to simulated images using the HOMO and LUMO alone. Especially in the case of the LUMO, this does result in a brightening of the acetylene contrast, though also in an increase in intramolecular structure beyond what is observed. Secondly, multiple values of the ferrocene–ferrocene dihedral angle intermediate between *cis* and *trans* geometries were used. Moderate twisting ( $60\text{--}90^\circ$ ) away from *trans* results in a better match between simulation and experiment for both occupied and unoccupied states. Not only do the approximations made in the theoretical calculations caution against making a precise assignment of geometry, but Fig. 9 shows only some experimental sensitivity to the torsion angle. This is in line with Heinrich *et al.*, who have shown that tilt of ferrocenes is difficult to decipher from experimental STM images alone.<sup>36</sup>

Overall, then, the symmetry of the experimental images and the comparison with theory suggest a adsorption geometry for DFA that is intermediate between *cis* and *trans*. This is not the geometry that would maximize Cp–surface  $\pi$ -electron interactions, and it is also in contrast to X-ray crystallographic data, which show bulk DFA is in a *trans* conformation.<sup>62</sup> Since ferrocene and diferrocene complexes adsorption geometries

are influenced by the substrate, we must consider all the components of the environment when assessing and explaining the adsorption geometry of DFA and benzene on Au(111). Benzene has previously been reported to physisorb parallel to the Au(111) surface, with multilayers of benzene standing up perpendicular to both the surface and the initial monolayer of benzene in order to maximize intermolecular  $\pi$ -bonding of the benzene in the second layer.<sup>52,57,58</sup> It is quite possible that we see DFA physisorbed with the Cp rings perpendicular to the surface in order to maximize interactions between neighboring DFA molecules. Studies of bulk ferrocene have found that the Cp rings of ferrocene prefer to pack perpendicular to one another, with the hydrogens of the Cp ring adjacent to the Fe center of the neighboring ferrocene.<sup>59–61</sup> We do not see the DFA packing perpendicular to one another, but an underlying benzene monolayer may stabilize the DFA causing it to physisorb in a specific manner.

In general, we would not expect a gas-phase electronic-structure calculation to adequately model the electronic state density of a molecule adsorbed on a metal surface; a correct treatment would necessarily include the surface, as well as a more appropriate selection of the DFT functional to more accurately describe dispersive forces.<sup>66–69</sup> Given that our calculations do not include the surface or the STM tip, even this qualitative level of agreement between the calculated and experimental images is perhaps surprising. A number of particular properties of the DFA–benzene–Au(111) system may contribute to de-emphasizing the contribution of the surface to the STM image: the ferrocene groups are rigid, and the DFA adsorbed in such a way that molecule–molecule interactions determine geometry more than molecule–surface interactions. Furthermore, the adsorption of DFA atop a benzene monolayer will isolate the molecule from the surface, and the high-contrast features in STM images—the  $\pi$ -electron systems of the ferrocene groups and the acetylene linker—will be relatively unperturbed by the underlying substrate.

The DFA–benzene–Au(111) adsorption system is complex, and it would be possible for this to result in a wide range of different adsorption geometries, potentially dependent on the DFA density as well as the coverage and relative positions of neighboring benzene molecules. In contrast to this, we observe similar molecular features in STM images under a variety of different conditions. One example is presented in Fig. 10, which shows both positive-bias and negative-bias of DFA. In these images, the DFA molecules appear quite similar across the image; most notably, the loosely agglomerated molecules in the area on the right side of each image give nearly identical features to molecules close-packed in the left side of each image. This behavior suggests that after taking into account the sensitivity of the STM to molecular orientation, local intermolecular interactions are unlikely to be strong perturbers of the DFA adsorption geometry. As a final probe of the benzene–DFA interaction, we also pulse-deposited DFA from solution in diethyl ether, with images shown in Fig. 11. While observed images are not identical, the general trends remain of more compact and symmetric features at negative bias voltages and larger, point-symmetric features at positive bias.

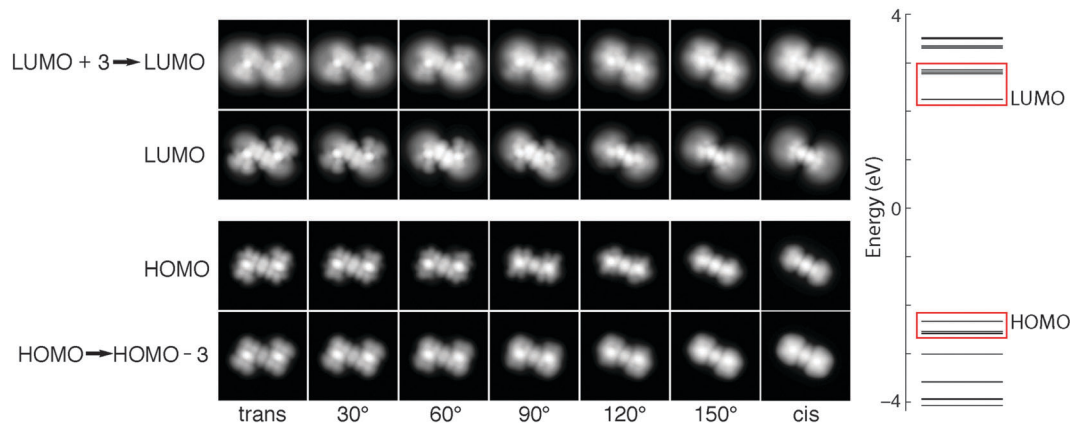


**Fig. 9** Simulated STM images for various torsional geometries intermediate between *trans* and *cis*; in all cases, molecules were aligned with their  $C_2$  axis normal to the surface. The effect of averaging over multiple electronic states (LUMO vs. LUMO to LUMO + 3; HOMO vs. HOMO to HOMO - 3) is also shown. Calculated energies for the electronic states used are shown on the right.

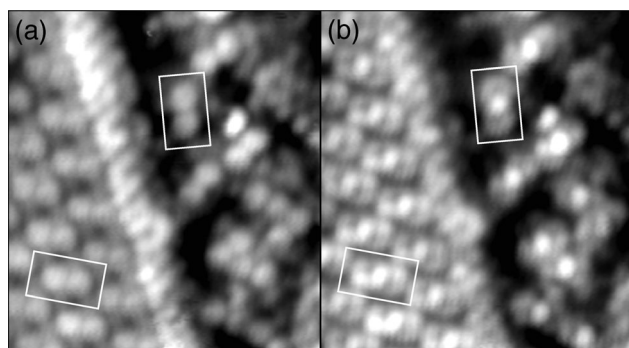


**Fig. 10** (a) and (b)  $76 \text{ \AA} \times 83 \text{ \AA}$ , images of both (a), OMOs, and (b), UMOs, of tightly and loosely packed DFA. Image (a) was scanned with a sample bias voltage of  $-1.0 \text{ V}$  and a tunneling current of  $10 \text{ pA}$ . Image (b) was scanned with a sample bias voltage of  $+1.0 \text{ V}$  and a tunneling current of  $10 \text{ pA}$ .

These similarities indicate that the benzene–DFA interaction is not the main determinant of DFA adsorption geometry.

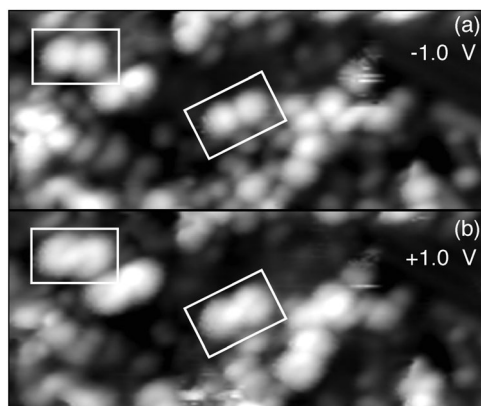


**Fig. 11** (a) and (b)  $112 \text{ \AA} \times 48 \text{ \AA}$ , images of both (a), OMOs, and (b), UMOs, of DFA pulse-deposited with (and therefore coadsorbed with) diethyl ether. Image (a) was scanned with a sample bias voltage of  $-1.0 \text{ V}$  and a tunneling current of  $10 \text{ pA}$ . Image (b) was scanned with a sample bias voltage of  $+1.0 \text{ V}$  and a tunneling current of  $10 \text{ pA}$ . The asymmetry and general features of the imaged molecules are similar to that observed with benzene solvent.

In conclusion, pulse-deposition of DFA results in intact molecular adsorption adjacent to and on top of benzene on Au(111). Simple DFT calculations, excluding the STM tip and the surface, agree qualitatively with experimental data, suggesting that the DFA is not strongly interacting with the Au(111) surface. STM images, supported by DFT calculations, suggest that when partial monolayers of DFA are adsorbed on benzene, the DFA adsorbs with a ferrocene–ferrocene dihedral angle intermediate between *trans* and *cis*.

## Acknowledgements

This work was supported by the National Science Foundation under NSF CHE-1124762.

## References

- 1 T. J. Kealy and P. L. Pauson, *Nature*, 1951, **168**, 1039–1040.
- 2 E. Hillard, A. Vessieres, L. Thouin, G. Jaouen and C. Amatore, *Angew. Chem., Int. Ed.*, 2006, **45**, 285–290.
- 3 A. Nguyen, A. Vessieres, E. A. Hillard, S. Top, P. Pigeon and G. Jaouen, *Chimia*, 2007, **61**, 716–724.
- 4 A. I. Mufula, B. A. Aderibigbe, E. W. Neuse and H. E. Mukaya, *J. Inorg. Organomet. Polym. Mater.*, 2012, **22**, 423–428.
- 5 B. Fabre, *Acc. Chem. Res.*, 2010, **43**, 1509–1518.
- 6 M. Even, B. Heinrich, D. Guillon, D. Guldi, M. Prato and R. Deschenaux, *Chem.–Eur. J.*, 2001, **7**, 2595–2604.
- 7 P. Stepnicka, *Eur. J. Inorg. Chem.*, 2005, 3787–3803.
- 8 R. G. Arrayas, J. Adrio and J. C. Carretero, *Angew. Chem., Int. Ed.*, 2006, **45**, 7674–7715.
- 9 R. Atkinson, V. Gibson and N. Long, *Chem. Soc. Rev.*, 2004, **33**, 313–328.
- 10 L. Dai, T. Tu, S. You, W. Deng and X. Hou, *Acc. Chem. Res.*, 2003, **36**, 659–667.
- 11 C. LeVanda, D. Cowan, C. Leitch and K. Bechgaard, *J. Am. Chem. Soc.*, 1974, **96**, 6788–6789.

- 12 C. LeVanda, K. Bechgaard and D. O. Cowan, *J. Org. Chem.*, 1976, **41**, 2700–2704.
- 13 J. Kramer and D. Hendrickson, *Inorg. Chem.*, 1980, **19**, 3330–3337.
- 14 W. S. Hammack, H. G. Drickamer, M. D. Lowery and D. N. Hendrickson, *Inorg. Chem.*, 1988, **27**, 1307–1308.
- 15 R. Nielson, L. Lyon and J. Hupp, *Inorg. Chem.*, 1996, **35**, 970–973.
- 16 A. Vlad, M. Cazacu, C. Turta, R. I. Tigoianu, A. Airinei and A. Arvinte, *Synth. Met.*, 2012, **161**, 2659–2668.
- 17 Y. Lu, R. Quardokus, C. S. Lent, F. Justaud, C. Lapinte and S. A. Kandel, *J. Am. Chem. Soc.*, 2010, **132**, 13519–13524.
- 18 R. C. Quardokus, Y. Lu, N. A. Wasio, C. S. Lent, F. Justaud, C. Lapinte and S. A. Kandel, *J. Am. Chem. Soc.*, 2012, **134**, 1710–1714.
- 19 W. Y. Man, K. B. Vincent, H. J. Spencer, D. S. Yufit, J. A. K. Howard and P. J. Low, *J. Cluster Sci.*, 2012, **23**, 853–872.
- 20 J.-L. Xia, W. Y. Man, X. Zhu, C. Zhang, G.-J. Jin, P. A. Schauer, M. A. Fox, J. Yin, G.-A. Yu, P. J. Low and S. H. Liu, *Organometallics*, 2012, **31**, 5321–5333.
- 21 M. A. Fox, B. Le Guennic, R. L. Roberts, D. A. Brue, D. S. Yufit, J. A. K. Howard, G. Manca, J.-F. Halet, F. Hartl and P. J. Low, *J. Am. Chem. Soc.*, 2011, **133**, 18433–18446.
- 22 K. Costuas, O. Cadour, F. Justaud, S. Le Stang, F. Paul, A. Monari, S. Evangelisti, L. Toupet, C. Lapinte and J.-F. Halet, *Inorg. Chem.*, 2011, **50**, 12601–12622.
- 23 F. Justaud, T. Roisnel and C. Lapinte, *New J. Chem.*, 2011, **35**, 2219–2226.
- 24 K. Costuas and S. Rigaut, *Dalton Trans.*, 2011, **40**, 5643–5658.
- 25 W. Y. Man, J.-L. Xia, N. J. Brown, J. D. Farmer, D. S. Yufit, J. A. K. Howard, S. H. Liu and P. J. Low, *Organometallics*, 2011, **30**, 1852–1858.
- 26 N. A. Wasio, R. C. Quardokus, R. P. Forrest, S. A. Corcelli, Y. Lu, C. S. Lent, F. Justaud, C. Lapinte and S. A. Kandel, *J. Phys. Chem. C*, 2012, **116**, 25486–25492.
- 27 R. F. Dou, D. Y. Zhong, W. C. Wang, K. Wedeking, G. Erker, L. Chi and H. Fuchs, *J. Phys. Chem. C*, 2007, **111**, 12139–12144.
- 28 K. Wedeking, Z. Mu, G. Kehr, R. Frohlich, G. Erker, L. Chi and H. Fuchs, *Langmuir*, 2006, **22**, 3161–3165.
- 29 K. Wedeking, Z. Mu, G. Kehr, J. Sierra, C. Lichtenfeld, S. Grimme, G. Erker, R. Frohlich, L. Chi, W. Wang, D. Zhong and H. Fuchs, *Chem.–Eur. J.*, 2006, **12**, 1618–1628.
- 30 D. Y. Zhong, W. C. Wang, R. F. Dou, K. Wedeking, G. Erker, L. F. Chi and H. Fuchs, *Phys. Rev. B: Condens. Matter Mater. Phys.*, 2007, **76**, 205428.
- 31 C. Waldfried, D. Welipitiya, C. Hutchings, H. deSilva, G. Gallup, P. Dowben, W. Pai, J. Zhang, J. Wendelken and N. Boag, *J. Phys. Chem. B*, 1997, **101**, 9782–9789.
- 32 D. Welipitiya, P. Dowben, J. Zhang, W. Pai and J. Wendelken, *Surf. Sci.*, 1996, **367**, 20–32.
- 33 C. Woodbridge, D. Pugmire, R. Johnson, N. Boag and M. Langell, *J. Phys. Chem. B*, 2000, **104**, 3085–3093.
- 34 D. Zhong, K. Wedeking, T. Bloemker, G. Erker, H. Fuchs and L. Chi, *ACS Nano*, 2010, **4**, 1997–2002.
- 35 K. F. Braun, V. Iancu, N. Pertaya, K. H. Rieder and S. W. Hla, *Phys. Rev. Lett.*, 2006, **96**, 246102.
- 36 B. W. Heinrich, L. Limot, M. V. Rastei, C. Iacovita, J. P. Bucher, D. M. Djimbi, C. Massobrio and M. Boero, *Phys. Rev. Lett.*, 2011, **107**, 216801.
- 37 D. Y. Zhong, J. Franke, T. Bloemker, G. Erker, L. F. Chi and H. Fuchs, *Nano Lett.*, 2009, **9**, 132–136.
- 38 J. Jiao, G. Long, L. Rebbouh, F. Grandjean, A. Beatty and T. Fehner, *J. Am. Chem. Soc.*, 2005, **127**, 17819–17831.
- 39 S. Guo and S. A. Kandel, *J. Chem. Phys.*, 2008, **128**, 014702.
- 40 R. K. Dieter, L. A. Silks, J. R. Fishpaugh and M. E. Kastner, *J. Am. Chem. Soc.*, 1985, **107**, 4679–4692.
- 41 D. Guillaneux and H. B. Kagan, *J. Org. Chem.*, 1995, **60**, 2502–2505.
- 42 G. Doisneau, G. Balavoine and T. Fillerbeenkhan, *J. Organomet. Chem.*, 1992, **425**, 113–117.
- 43 M. Rosenblum, N. Brawn, J. Papenmeier and M. Applebaum, *J. Organomet. Chem.*, 1966, **6**, 173–180.
- 44 T. Kanno, H. Tanaka, T. Nakamura, H. Tabata and T. Kawai, *Jpn. J. Appl. Phys.*, 1999, **38**, L606–L607.
- 45 R. Bernard, V. Huc, P. Reiss, F. Chandezon, P. Jegou, S. Palacin, G. Dujardin and G. Comtet, *J. Phys.: Condens. Matter*, 2004, **16**, 7565–7579.
- 46 L. Grill, I. Stass, K. H. Rieder and F. Moresco, *Surf. Sci.*, 2006, **600**, L143–L147.
- 47 Y. Shirai, A. J. Osgood, Y. M. Zhao, K. F. Kelly and J. M. Tour, *Nano Lett.*, 2005, **5**, 2330–2334.
- 48 Y. Terada, B. K. Choi, S. Heike, M. Fujimori and T. Hashizume, *Nano Lett.*, 2003, **3**, 527–531.
- 49 Y. Terada, B. K. Choi, S. Heike, M. Fujimori and T. Hashizume, *J. Appl. Phys.*, 2003, **93**, 10014–10017.
- 50 M. Valiev, E. J. Bylaska, N. Govind, K. Kowalski, T. P. Straatsma, H. J. J. Van Dam, D. Wang, J. Nieplocha, E. Apra, T. L. Windus and W. de Jong, *Comput. Phys. Commun.*, 2010, **181**, 1477–1489.
- 51 J. Tersoff and D. R. Hamann, *Phys. Rev. B: Condens. Matter Mater. Phys.*, 1985, **31**, 805–813.
- 52 E. C. H. Sykes, B. A. Mantooth, P. Han, Z. J. Donhauser and P. S. Weiss, *J. Am. Chem. Soc.*, 2005, **127**, 7255–7260.
- 53 L. Bartels, G. Meyer and K. H. Rieder, *Phys. Rev. Lett.*, 1997, **79**, 697–700.
- 54 J. G. Kushmerick, S. A. Kandel, P. Han, J. A. Johnson and P. S. Weiss, *J. Phys. Chem. B*, 2000, **104**, 2980–2988.
- 55 S. J. Stranick, M. M. Kamna and P. S. Weiss, *Science*, 1994, **266**, 99–102.
- 56 S. J. Stranick, M. M. Kamna and P. S. Weiss, *Surf. Sci.*, 1995, **338**, 41–59.
- 57 P. Jakob and D. Menzel, *Surf. Sci.*, 1989, **220**, 70–95.
- 58 B. A. Mantooth, E. C. H. Sykes, P. Han, A. M. Moore, Z. J. Donhauser, V. H. Crespi and P. S. Weiss, *J. Phys. Chem. C*, 2007, **111**, 6167–6182.
- 59 D. Braga and F. Grepioni, *Organometallics*, 1992, **11**, 711–718.
- 60 F. Maharaj, A. McDonagh, M. Scudder, D. Craig and I. Dance, *Crystengcomm*, 2003, **5**, 305–309.
- 61 D. Zhong, K. Wedeking, T. Bloemker, G. Erker, H. Fuchs and L. Chi, *ACS Nano*, 2010, **4**, 1997–2002.

- 62 M. Katora, D. Necas and P. Stepnicka, *Collect. Czech. Chem. Commun.*, 2003, **68**, 1897–1903.
- 63 L. Vernisse, S. Munery, N. Ratel-Ramond, Y. Benjalal, O. Guillermet, X. Bouju, R. Coratger and J. Bonvoisin, *J. Phys. Chem. C*, 2012, **116**, 13715–13721.
- 64 S. Munery, N. Ratel-Ramond, Y. Benjalal, L. Vernisse, O. Guillermet, X. Bouju, R. Coratger and J. Bonvoisin, *Eur. J. Inorg. Chem.*, 2011, 2698–2705.
- 65 R. J. Hamers, *Annu. Rev. Phys. Chem.*, 1989, **40**, 531–559.
- 66 T. S. Chwee and M. B. Sullivan, *J. Chem. Phys.*, 2012, **137**, 134703.
- 67 M. Dion, H. Rydberg, E. Schroder, D. Langreth and B. Lundqvist, *Phys. Rev. Lett.*, 2004, **92**, 246401.
- 68 B. Hammer, L. Hansen and J. Norskov, *Phys. Rev. B: Condens. Matter Mater. Phys.*, 1999, **59**, 7413–7421.
- 69 K. Tonigold and A. Gross, *J. Chem. Phys.*, 2010, **132**, 224701.